

Integration of a deep-learning-based fire model into a global land surface model

Rackhun Son¹, Tobias Stacke², Veronika Gayler², Julia Esther Marlene Sophia Nabel², Reiner Schnur³, Lazaro Alonso Silva¹, Christian Requena Mesa⁴, Alexander Winkler¹, Stijn Hantson⁵, Sönke Zaehle¹, Ulrich Weber⁶, and Nuno Carvalhais⁷

¹Max Planck Institute for Biogeochemistry

²Max Planck Institute for Meteorology

³Max Planck Institute for Meteorology

⁴Unknown

⁵University of California, Irvine

⁶Max-Planck Institute for Biogeochemistry

⁷MPI-Jena

March 16, 2023

Abstract

Fire is a crucial factor in terrestrial ecosystems playing a role in disturbance for vegetation dynamics. Process-based fire models quantify fire disturbance effects in stand-alone dynamic global vegetation models (DGVMs) and their advances have incorporated both descriptions of natural processes and anthropogenic drivers. Nevertheless, these models show limited skill in modeling fire events at the global scale, due to stochastic characteristics of fire occurrence and behavior as well as the limits in empirical parameterizations in process-based models. As an alternative, machine learning has shown the capability of providing robust diagnostics of fire regimes. Here, we develop a deep-learning-based fire model (DL-fire) to estimate daily burnt area fraction at the global scale and couple it within JSBACH4, the land surface model used in the ICON ESM. The stand-alone DL-fire model forced with meteorological, terrestrial and socio-economic variables is able to simulate global total burnt area, showing 0.8 of monthly correlation (rm) with GFED4 during the evaluation period (2011-15). The performance remains similar with the hybrid modeling approach JSB4-DL-fire (rm=0.79) outperforming the currently used uncalibrated standard fire model in JSBACH4 (rm=-0.07). We further quantify the importance of each predictor by applying layer-wise relevance propagation (LRP). Overall, land properties, such as fuel amount and water content in soil layers, stand out as the major factors determining burnt fraction in DL-fire, paralleled by meteorological conditions over tropical and high latitude regions. Our study demonstrates the potential of hybrid modeling in advancing fire prediction in ESMs by integrating deep learning approaches in physics-based dynamical models.

Hosted file

958429_0_art_file_10796588_rrt49t.docx available at <https://authorea.com/users/596143/articles/629772-integration-of-a-deep-learning-based-fire-model-into-a-global-land-surface-model>

Hosted file

958429_0_supp_10796633_rrt4y1.docx available at <https://authorea.com/users/596143/articles/629772-integration-of-a-deep-learning-based-fire-model-into-a-global-land-surface-model>

1 **Integration of a deep-learning-based fire model into a global land surface model**

2
3 **Authors: Rackhun Son^{1,*}, Tobias Stacke², Veronika Gayler², Julia E.M.S. Nabel^{1,2}, Reiner**
4 **Schnur², Lazaro Alonso Silva¹, Christian Requena-Mesa¹, Alexander J. Winkler¹, Stijn**
5 **Hantson³, Sönke Zaehle¹, Ulrich Weber¹ and Nuno Carvalhais^{1,4,5}**

6 ¹Max Planck Institute for Biogeochemistry, Jena, Germany.

7 ²Max Planck Institute for Meteorology, Hamburg, Germany.

8 ³Faculty of Natural Sciences, Universidad del Rosario, Bogotá, Colombia.

9 ⁴ELLIS Unit Jena, Jena, Germany.

10 ⁵Departamento de Ciências e Engenharia do Ambiente, Faculdade de Ciências e Tecnologia,
11 Universidade Nova de Lisboa, Caparica, Portugal.

12
13 *Correspondence to: Rackhun Son (rackhun@bgc-jena.mpg.de)

16 **Key Points:**

- 17 • Deep neural networks (DNN) can accurately predict global burnt area fraction on a daily
18 scale.
- 19 • Integration of the DNN in a physics-based land model significantly improves fire-driven
20 loss in vegetation dynamics.
- 21 • The DNN accounts for regional fire variations by assigning varying degrees of
22 importance to each predictor.
23

24 **Abstract**

25 Fire is a crucial factor in terrestrial ecosystems playing a role in disturbance for
26 vegetation dynamics. Process-based fire models quantify fire disturbance effects in stand-alone
27 dynamic global vegetation models (DGVMs) and their advances have incorporated both
28 descriptions of natural processes and anthropogenic drivers. Nevertheless, these models show
29 limited skill in modeling fire events at the global scale, due to stochastic characteristics of fire
30 occurrence and behavior as well as the limits in empirical parameterizations in process-based
31 models. As an alternative, machine learning has shown the capability of providing robust
32 diagnostics of fire regimes. Here, we develop a deep-learning-based fire model (DL-fire) to
33 estimate daily burnt area fraction at the global scale and couple it within JSBACH4, the land
34 surface model used in the ICON ESM. The stand-alone DL-fire model forced with
35 meteorological, terrestrial and socio-economic variables is able to simulate global total burnt
36 area, showing 0.8 of monthly correlation (r_m) with GFED4 during the evaluation period (2011-
37 15). The performance remains similar with the hybrid modeling approach JSB4-DL-fire
38 ($r_m=0.79$) outperforming the currently used uncalibrated standard fire model in JSBACH4 ($r_m=-$
39 0.07). We further quantify the importance of each predictor by applying layer-wise relevance
40 propagation (LRP). Overall, land properties, such as fuel amount and water content in soil layers,
41 stand out as the major factors determining burnt fraction in DL-fire, paralleled by meteorological
42 conditions over tropical and high latitude regions. Our study demonstrates the potential of hybrid
43 modeling in advancing fire prediction in ESMs by integrating deep learning approaches in
44 physics-based dynamical models.

45

46 **Plain Language Summary**

47 We develop a fire-vegetation model based on a hybrid approach integrating artificial
48 intelligence (AI) techniques into physics-based models. Given the weather conditions, vegetation
49 states, and human factors, our model estimates daily burned area fraction. The spatiotemporal
50 variations in burned area are closely reproduced, especially over fire-prone regions, such as
51 Africa, South America, and Australia. Our model is able to represent regional variations in the
52 drivers of fire occurrence, showing different importance of input predictors for different regions.

53 This approach shows the possibilities of using deep learning (DL) models to provide in-depth
54 fire predictions in Earth system models.

55

56 **1. Introduction**

57 Fire is one of the main natural vegetation disturbance agents, and as such, a primary
58 interactive component in the terrestrial ecosystem. Biomass burning affects the structure and
59 dynamics of ecological processes (McLauchlan et al., 2020). Fire emissions alter atmospheric
60 composition of trace gases and aerosol particles (Koppmann et al., 2005), with subsequent
61 influences on land surface albedo (López-Saldaña et al., 2015), energy budgets (F. Li et al.,
62 2017), climate (Liu et al., 2019; Voulgarakis & Field, 2015) and global biogeochemical cycles
63 (Carcaillet et al., 2002; Crutzen & Andreae, 1990). Present-day global carbon emissions due to
64 fire are approximately 1.5-3.0 PgC/yr (van der Werf et al., 2017). There is ample evidence that
65 climate change has already resulted in increased fire risk and burned area in various areas around
66 the world, and future increases are expected due to climate change (Seidl et al., 2017; Son et al.,
67 2021). As fires are a significant source of greenhouse gases, there is the potential for positive
68 (Harrison et al., 2018; Kurz et al., 1995) and negative feedbacks (Mahowald, 2011; Ward et al.,
69 2012). Yet, important uncertainties remain to adequately represent fires in Earth system models
70 (ESMs), with uncertainties in the representation of fire disturbance still dominating the overall
71 uncertainties in the estimation of carbon fluxes from land (Hardouin et al., 2022).

72 Global fire models have been developed based on empirical and physical understanding
73 of the fire process, and these have been incorporated within dynamic global vegetation models
74 (DGVMs) (Hantson et al., 2016). In the early stage of global fire modeling, burnt area was
75 estimated based on the amount of dry fuel and the length of fire season (Thonicke et al., 2001).
76 The representation of frequency of fire occurrence was advanced by considering weather-driven
77 fire risk (Lenihan, 1998). Venevsky et al. (2002) added characteristics of fire spread by adopting
78 the Rothermel's rate-of-spread (RoS) equations (Rothermel, 1972). Based on the RoS, more
79 advanced fire related physical representations were introduced (Pfeiffer et al., 2013; Thonicke et
80 al., 2010) and implemented in various DGVMs (Drüke et al., 2019; Lasslop et al., 2014; Yue et
81 al., 2016). Human activity impacts are also considered as nonlinear functions for fire ignition and

82 suppression based on population density, gross domestic product (GDP) and land-use changes
83 (Kloster et al., 2010; le Page et al., 2015; F. Li et al., 2013).

84 Although there has been remarkable progress in global fire modeling, there are still many
85 challenges remaining to represent the fire process and fire-vegetation interactions. For instance,
86 fire characteristics, such as the completeness of combustion and plant mortality, are not robustly
87 parameterized to reflect differences depending on vegetation types (Lasslop et al., 2014).
88 Uncertainties in vegetation effects on fire remain as a main drawback in DGVMs (Forkel et al.,
89 2019). Besides, while fire modeling has advanced with more sophisticated process based
90 representations, there is still no agreement on the optimal level of complexity for a global fire
91 model (Hantson et al., 2016).

92 Deep learning (DL), as a subset of machine learning (ML), has recently been
93 incorporated in fire studies leading to significant advances within different aspects of fire
94 science. For instance, spatial behavior of fire was successfully captured by using convolutional
95 neural networks (Hodges & Lattimer, 2019; Radke et al., 2019). The long short-term memory
96 modeling (LSTM) approaches also showed capability of predicting fire damage and duration (Z.
97 Li et al., 2021; Liang et al., 2019). To address the spatiotemporal context for wildfire danger,
98 (Kondylatos et al., 2022) applied a convolutional-LSTM network (Shi et al., 2015) integrating
99 meteorological, environmental, and anthropogenic drivers. Other studies leveraged ML/DL
100 methods to characterize various aspects of fire occurrence, such as fire weather (Son et al.,
101 2022), lightning ignition (Coughlan et al., 2021), fire susceptibility (Zhang et al., 2021) and fuel
102 availability (D'Este et al., 2021).

103 In this study, we develop a DL-based global fire model to improve biomass burnt damage
104 simulation within a land surface model. Our model is composed of three independent modules to
105 represent weather driven fire danger, land properties and anthropogenic effects on burnt area
106 fraction estimation. Compared to a previous DL surrogate fire model (Zhu et al., 2022), our
107 study has advances in two folds: 1) we incorporate LSTM based recurrent model architecture to
108 consider time dependent memory effects from dynamic weather and vegetation processes; and 2)
109 our model training was based on observational datasets, except for fuel load, allowing it to be
110 coupled with any DGVM.

111

112 2. Methodology and Data

113 2.1. JSBACH4 and its simple fire scheme

114 JSBACH4 (Jena Scheme for Biosphere-Atmosphere Coupling in Hamburg version 4),
 115 which is the land surface model used in the ICON ESM, incorporates a simple fire model
 116 implemented to estimate fire damage based on combustible fuel availability and fuel dryness
 117 (Jungclaus et al., 2022). As one of the most simple fire representations, it can be applied in any
 118 global land surface model. The primary objective of the fire scheme is more focused on the
 119 disturbance effect on natural land cover changes, rather than fire occurrence and interactions,
 120 limiting its role on vegetation dynamics and carbon cycling in ecosystems. Instead, the previous
 121 version of JSBACH (JSBACH3.2) used the SPITFIRE fire model (Thonicke et al., 2010) to
 122 simulate global fire regimes, but it has not yet been implemented in JSBACH4.

123 In the simple fire scheme, the fuel availability is represented by the total litter density (L)
 124 and is compared to the litter threshold (L_0). The fuel dryness is estimated from surface level air
 125 relative humidity ($\overline{rh_t}$) smoothed with a persistence factor at each time step (Eq.1). When the
 126 humidity decreases lower than its threshold (rh_0), the fraction of burned area (FBA) is assumed
 127 to linearly increase as humidity decreases:

$$129 \quad \overline{rh_t} = \overline{rh_{t-1}} \times p + \min(rh_t, 100) \times (1 - p), \quad p = 0.95^{\frac{1}{48}} \quad (1)$$

$$130 \quad FBA = FBA_{min} + \frac{1}{\tau} \times \frac{rh_0 - \overline{rh_t}}{rh_0} \quad \text{if } L > L_0 \text{ and } rh < rh_0 \quad \text{otherwise } 0 \quad (2)$$

131
 132 where, τ denotes the frequency of fire occurrence: set as 6 years for woody and 2 years
 133 for grass type vegetation. We take the simple fire model (hereafter referred to as JSB4-simple) as
 134 the baseline for model evaluation. The standalone version of JSBACH4 is used to run JSB4-
 135 simple with the default configurations as used in JSBACH3.2 and described in Reick et al.
 136 (2021).

137

138 2.2. Deep learning (DL) fire model

139 The deep learning fire model (DL-fire) is composed of three modules: weather-driven fire
 140 danger, land properties and anthropogenic effects (Figure 1). The development of the modules
 141 for weather danger (W-LSTM) and land properties (L-LSTM) are based on the long short-term

142 memory network approach (LSTM) (Hochreiter & Schmidhuber, 1997). LSTM is an advanced
 143 recursive neural network to handle temporal dynamic behaviors from sequential data. The key
 144 aspect of the LSTM approach is its memory unit, called cell state that maintains information on
 145 states over timesteps, and its update is regulated by input and forget gates:

$$146 \quad i_t = a_{sigmoid}(W_i \cdot [h_{t-1}, x_t] + b_i) \quad (3)$$

$$147 \quad f_t = a_{sigmoid}(W_f \cdot [h_{t-1}, x_t] + b_f) \quad (4)$$

$$148 \quad o_t = a_{sigmoid}(W_o \cdot [h_{t-1}, x_t] + b_o) \quad (5)$$

$$149 \quad \tilde{c}_t = \tanh(W_c \cdot [h_{t-1}, x_t] + b_c) \quad (6)$$

$$150 \quad c_t = f_t \odot c_{t-1} + i_t \odot \tilde{c}_t \quad (7)$$

$$151 \quad h_t = o_t \odot \tanh(c_t) \quad (8)$$

152

153 where i, f, o denote the input gate, forget gate, output gate and c, h denote cell and
 154 hidden state. The terms W and b refer to the weight matrices and bias vectors for each gate and
 155 the cell states (e.g. W_i is the matrix of weights for the input gate), $a_{sigmoid}$ is the sigmoid
 156 function, \tanh is the hyperbolic tangent function, and \odot denotes the element-wise product of
 157 vectors. The output dimension of the LSTM is set to 8 to be equal with the number of the plant
 158 functional types (PFTs), except for the bare land type.

159 The anthropogenic effect module uses two layers of fully connected feed-forward
 160 network:

161

$$162 \quad h_t = act(W_1 \cdot x_t + b_1) \quad (9)$$

$$163 \quad o_t = W_2 \cdot h_t + b_2 \quad (10)$$

164

165 where x denotes the input vector for anthropogenic variables and h is hidden layer
 166 vectors. The W and b terms are weight matrices and bias vectors for the input and hidden
 167 vectors. The function act represents a nonlinear transformation using a *softplus* function (Dugas
 168

169 et al., 2000) in this study. The vector o is the output vector of the anthropogenic effect module
 170 that has the same dimension as the outputs of the W-LSTM and L-LSTM modules.

171 The final output, the fraction of burned area, is the computed sum of all PFTs, except for
 172 the bare land type, after multiplying results of the three modules and the fractions of PFTs
 173 (orange vector in Figure 1). Also, we use the fraction of bare land (f_{bare}) and snow (f_{snow}),
 174 fuel (above ground plant litter in JSBACH4) and relative humidity not only as LSTM input
 175 predictors, but also as constraints on fire occurrence and intensity:

176

$$177 \quad FBA = (\sum o_w \times o_l \times o_a \times f_{PFTs}) \times \text{fire prone area} \times \text{dry fuel availability} \quad (11)$$

$$178 \quad \text{fire prone area} = 1 - f_{bare} - f_{snow} \quad (12)$$

$$179 \quad \text{dry fuel availability} = \text{fuel}_{norm} \times S\left(1 - \frac{rh}{100}\right) \quad \text{if } rh > rh_0 \quad \text{otherwise } 0 \quad (13)$$

$$180 \quad S(x) = \frac{1}{1 + e^{-20 \times (x - 0.5)}} \quad (14)$$

181

182 where o_w , o_l , o_a denote output vectors of W-LSTM, L-LSTM and anthropogenic effect
 183 modules and f_{PFTs} denotes the fractions of PFTs. We use sigmoidal curve function (S) to
 184 transform relative humidity into a non-linear space. rh_0 is the threshold of relative humidity for
 185 fire occurrence set as 60 (%), fuel_{norm} is normalized fuel using its maximum and minimum
 186 values during the training period (Eq.15).

187

188 **2.3. Burnt fraction**

189 For model training and evaluation, we used daily burned area from the Global Fire
 190 Emissions Database (GFED4) (Randerson et al., 2015) and calculated the burnt fraction for each
 191 grid cell. The GFED4 burned area product is based on the Moderate Resolution Imaging
 192 Spectroradiometer (MODIS) Collection 5.1 (MCD64A1 v5.1), globally available at $0.25^\circ \times 0.25^\circ$
 193 spatial resolution.

194 Extreme data imbalance between instances of fire and no-fire is observed over all regions
 195 (Table 1). If the data with a large proportion of no-fire instances are directly used for model
 196 training, it is highly likely to mislead model outputs to converge into zero values. In order to
 197 reduce the risk of zero convergence, we adopt two strategies. We first used a gaussian kernel
 198 with 30 days of window size to smooth the burned area (step1 in Table 1). Subsequently, we

199 downsample no-fire instances according to ratios in Table 1 (step2 ratio), reducing the
200 imbalanced ratios to be close to 1:1 for all regions.

201

202 **2.4. Input variables**

203 The DL-fire uses 50 predictors which are divided into three sub-modules to predict burnt
204 fraction illustrated in detail in Table 2. The weather danger module (W-LSTM) uses 9 predictors,
205 including anomalies of temperature, specific and relative air humidity. Weather variables, such
206 as temperature, specific/relative air humidity, wind speed and precipitation, are obtained from
207 ERA5 (Hersbach et al., 2020) and lightning climatology is based on a dataset from the
208 spaceborne Optical Transient Detector (OTD) and Lightning Imaging Sensor (LIS) on the
209 Tropical Rainfall Measuring Mission (TRMM) satellite (Cecil et al., 2014). The anomalies are
210 calculated by extracting daily climatology (mean values on a day of year basis) during the years
211 1950-2020.

212 The land property module (L-LSTM) takes 23 predictors including the water volumes in
213 four soil layers are obtained from ERA5-Land (Muñoz-Sabater et al., 2021) and the Leaf Area
214 Index (LAI) is derived from the collection-5 MODIS LAI product (Myneni et al., 2015). We also
215 calculate daily anomalies for the water volumes and LAI using the above mentioned method
216 during 1950-2020 and 2003-2020, respectively. The topographic factors, such as elevation, slope
217 and roughness, are taken from (Amatulli et al., 2018). The amount of fuel is simulated by JSB4-
218 simple. The area distributions of plant functional types (PFTs) are obtained from Pongratz et al.
219 (2008), given as inputs for running JSBACH4 and we remap PFTs to be nine types as outlined in
220 Table 2.

221 The anthropogenic effect module (A-NN) takes into account a total of 18 predictors from
222 five different characteristics: population density (Klein Goldewijk et al., 2017), gross domestic
223 product (GDP) and human development index (HDI) (Kummu et al., 2018), total road density
224 (Meijer et al., 2018) and 14 fractions representing the state of land use (Hurtt et al., 2020).

225 All the input variables are regridded and aggregated to a daily timestep and 0.25 degree
226 spatial resolution to be consistent with the GFED4. Except for PFT fractions constrained in the
227 range of [0,1], we normalized predictors using maximum and minimum values of each region
228 based on the training period ($x_{r,train_max}$ and $x_{r,train_min}$, where r denotes a GFED region in
229 Figure S1), ideally to be in the range of [0,1]:

230

$$231 \quad (x - x_{r,train_{min}})/(x_{r,train_{max}} - x_{r,train_{min}}) \quad (15)$$

232

233 **2.5. Model setup for training and simulation with JSBACH4**

234 We develop 14 regional models based on GFED reference regions (Figure S1). To train
 235 the models, we use 12 years (2004-2015) of data considering data availability for burnt fraction
 236 and all the input predictors. We randomly select 80% of the dataset from the first 7 years (2004-
 237 10) for training and the remaining 20% are for validation during the model training stage. We
 238 apply a stratified random sampling approach is applied to preserve the same ratios between
 239 fire/no-fire incidents. The last 5 years (2011-15) are used for performance evaluation.

240 The dimension of the hidden layer is set to be 64 for all the three module architectures
 241 and dropout regularization is implemented for the anthropogenic module layers with 10% of
 242 probability to randomly inactivate neural network nodes. For the LSTM modules, the sequence
 243 length of training dataset is set to 14 days. We use the mean square error (MSE) loss function
 244 with ADAM optimizer (Kingma & Ba, 2014) by setting the learning rate to 0.001 and batch size
 245 to 1024. To avoid overfitting on the train dataset, we stop model training after a span of 30
 246 epochs where no further improvement is observed in the validation dataset.

247 The DL-fire is trained without coupling to the dynamics of JSBACH4, as an offline
 248 learning approach. When the DL-fire is integrated into JSBACH4, all the land properties are
 249 provided by physics-based dynamics processes, except for topography. The other predictors are
 250 set to be forced by datasets used for model training and it allows the evaluation of simulation
 251 results from the year 2001. We perform experiments on the R2B4 ICON-grid system with spin-
 252 up time of 51 years, starting from the year 1950, and evaluate simulation results from 2001 to
 253 2015. During the spin-up period (before the year 2001), we set all anthropogenic variables to be
 254 static at the state of January 1st 2001.

255

256 **2.6. Evaluation metrics**

257 To quantify the performance in simulating spatial variation, we apply the normalized
 258 mean error (NME) with area weights suggested by (Hantson et al., 2020):

259

$$260 \quad NME = \sum_i A_i |o_i - m_i| / \sum_i A_i |o_i - \bar{o}| \quad (15)$$

261

262 where o_i denotes the observed value, m_i the simulated value and A_i cell area at grid cell i .

263 \bar{o} is the mean of the observed values. A smaller value of NME describes better agreement with

264 observation and zero is for perfect match between observation and model simulation. If NME is

265 larger than 1, model performance is worse than simple prediction with statistical mean value.

266 We calculate the Pearson correlation coefficient between daily (r_d), monthly (r_m) and

267 interannual (r_i) variability in predicted burnt fraction and GFED4, and the mean phase difference

268 (MPD) to evaluate seasonal variation (Kelley et al., 2013). To quantify a distance between two

269 phases, time unit is firstly transformed as an angle vector:

270

$$271 \theta_m = 2\pi(m - 1)/12 \quad (16)$$

272

273 where m denotes month (January-December). Then real (L_x) and imaginary (L_y)

274 component vectors are calculated by:

275

$$276 L_x = \sum_m x_m \cos(\theta_m) \quad (17)$$

$$277 L_y = \sum_m x_m \sin(\theta_m) \quad (18)$$

278

279 The phase (P) is described by direction of the vectors (Eq.19) and MPD quantifies the

280 phase difference by Eq.20:

281

$$282 P = \arctan(L_x/L_y) \quad (19)$$

$$283 MPD = \frac{1}{\pi} \sum_i A_i \times \arccos[\cos(\hat{P}_i - P_i)] / \sum_i A_i \quad (20)$$

284

285 where \hat{P}_i is phase from model simulation and P_i from observation at grid cell i .

286

287 2.7. Layer-wise relevance propagation

288 To interpret the decision making process of the DL-fire model, we apply the layer-wise

289 relevance propagation (LRP) (Bach et al., 2015) to decompose contributions from the input

290 space. LRP computes relevance scores for each individual input by propagating relevance from
291 the model output back through the neural network layers. While the total amount of relevance
292 scores in each layer is kept consistent, the relevance in a layer is redistributed to the previous
293 layer considering weights and input values, and this process repeats until getting the scores for
294 the input layer. Here, we normalized relevance scores for each timestep so that the absolute
295 values sum up to 1. Then we composite the normalized scores during the evaluation period to
296 compare relative attribution with a global aspect.

297

298 **3. Results**

299 **3.1. DL-fire model evaluation**

300 Globally, the predicted burnt fraction shows a good overall accordance with the GFED4
301 estimates during the evaluation period (Figs 2a, b) with a NME of 0.64 (Table 3). The pattern of
302 seasonal cycle is also accurately captured with 0.3 of MPD and 0.73 of r_d . Monthly aggregated
303 predictions show a higher correlation score ($r_m=0.80$) than a previous DL model (0.76) (Joshi &
304 Sukumar, 2021), although the evaluation period is different for both studies. However, high
305 fractions, especially in the second half of the years 2011 and 2012, are underestimated (Fig 2c)
306 indicating a degrading performance skill in interannual variability ($r_i=0.35$).

307 Regionally developed models vary in their performance skills. All the regional models
308 show a NME lower than 1.0 and the best score is achieved in the northern part of South America
309 (NHSA, 0.48), whereas NME is relatively high in regions where it shows large burnt fractions,
310 such as Boreal North America (BONA), the southern part of South America (SHSA), the
311 southern part of Africa (SHAF) and Central Asia (CEAS). The model for Central America
312 (CEAM) shows high predictability in seasonal variation with 0.19 of MPD, and the BONA,
313 SHSA, Africa and Equatorial Asia (EQAS) also perform well with a performance higher than 0.8
314 of r_d . The lowest daily correlations are obtained in the temperate North America (TENA, 0.47)
315 and CEAS (0.41), showing underestimations in each of the fire seasons (Figs S2b, k). 8 out of 14
316 regional models perform well on predicting interannual fire patterns with higher than 0.8 of r_i .
317 However, the least interannual predictability is shown across Southeast Asia (SEAS) and SHAF
318 ($r_i=-0.14, 0.08$) due to lack in detecting high burnt fractions (Figs S2i, l). These results,

319 especially due to the SHAF, cause considerable drop in the interannual predictability at the
320 global scale.

321

322 **3.2. Coupling with JSBACH4**

323 When the DL-fire model is coupled with JSBACH4 (JSB4-DL-fire), burnt fraction
324 prediction skill is significantly enhanced in comparison to the simple fire model (JSB4-simple).
325 JSB4-DL-fire improves NME score from 0.75 to 0.67 at the global scale, and NME decreases in
326 10 out of 14 regions (Table 4). Although burnt fractions in Africa and Siberia are
327 underestimated, JSB4-DL-fire successfully captures the spatial variation of burnt fraction,
328 especially across fire prone regions, such as Africa, South America, and Australia (Figs 3a, b).

329 Furthermore, burnt fractions in fuel-limited areas are improved to be close to zero in
330 JSB4-DL-fire. JSB4-simple sets nonzero constant parameter for the minimum degree of fire
331 damage (see Method), the results of JSB4-simple show higher than 0.1%/year of damage over
332 almost all areas, including deserts and extremely cold regions (Fig S3a). Due to this
333 oversimplified parameterization, arid areas and high latitudes, such as BONA, TENA, Europe
334 (EURO), Middle East (MIDE) and Asia (BOAS and CEAS), show poor NME scores (2.34, 2.49,
335 2.06, 6.10, 1.40 and 1.39, respectively). These discrepancies are effectively addressed by JSB4-
336 DL-fire with fuel and PFT constraints, improving NME to be lower than 1.0 across all the
337 regions, except for MIDE.

338 The global spatial variation in fire seasonality is compared by visualizing the month with
339 maximum fire damage per grid cell during the year 2001-15 (Figs 3c, d). JSB4-DL-fire shows
340 overall coincide fire season distribution with GFED4, and the best score of MPD is achieved
341 over CEAM (0.19, Table 4). Compared to JSB4-simple, the seasonal phase difference in AUST
342 is also improved (MPD=0.26), but JSB4-DL-fire achieves slightly increased scores in 8 out of 14
343 regions. Nevertheless, the most notable improvement in JSB4-DL-fire is found in temporal
344 correlations. While the global mean of the JSB4-simple simulation has a statistically
345 insignificant relationship with GFED4 ($r_d, r_m \approx 0$ and $r_i=0.17$), the JSB4-DL-fire considerably
346 increases the correlations ($r_d=0.61, r_m=0.79, r_i=0.37$). We also compare their seasonality during
347 2011-15 (DL evaluation period), showing that the month to month variability in JSB4-simple is

348 highly underestimated, showing a limited range in monthly burned area values, whereas spatial
349 and seasonal patterns of JSB4-DL-fire generally match well with GFED4 (Fig S4).

350 Regionally, the performance of JSB4-DL-fire is most marked in SHSA and SHAF (Figs
351 4e, i) with scores higher than 0.8 of r_d (Table 4). JSB4-DL-fire also effectively reduces
352 underestimation in NHAF and AUST (Figs 5h, n) as well as the overestimation in BONA, BOAS
353 and CEAS (Figs. 5a, i, k). Among 14 regions, JSB4-DL-fire enhances r_d in 9 and r_m in 12 of
354 them. In terms of interannual variability, the biggest improvement is found in BOAS, increasing
355 r_i from 0.1 to 0.76, whereas the variability in SEAS and MIDE are the least predictable (-0.04
356 and -0.12, respectively). Although JSB4-DL-fire outperforms JSB4-simple in general, in
357 comparison to the model validation results forced by observation (Table 3), the predictability of
358 DL-fire is degraded over almost all the regions by integrating with JSBACH4. These changes in
359 predictability by being coupled with JSBACH4 will be further discussed in terms of JSBACH4
360 internal biases in the next section.

361

362 **3.3. Model interpretation**

363 To understand how the DL fire model makes its predictions, we implement LRP for
364 evaluating the contribution of each predictor. Globally, the fraction of bare land shows the
365 highest absolute attribution with more than 16.3% of relevance score (Fig 5a). Its role, as a key
366 component in identifying no or low risk of fire, is highlighted across regions, where there are
367 large portions of arid lands or deserts, such as SHSA, MIDE, SHAF and AUST (Figs S5e, g, i,
368 n). Fuel load also shows a high ratio of contribution (14.1%) based on its multiple roles as a
369 constraint (7.4%) as well as an input of L-LSTM (6.7%). The volume of water in the 4th soil
370 layer (SWL4) counts as the 3rd key factor associated with fire severity in that it can be considered
371 an extreme condition when dryness has reached deeper soil level. Considering that the sum of
372 soil dryness-related variable scores occupies 34.4% of the total relevance, the changes in soil
373 dryness play as key drivers in the DL-fire.

374 Meteorological predictors, in spite of their small impacts in the global aspect (6.2%, Fig
375 5b), display significant importance in some tropical and high latitude regions. For instance,
376 tropical rain forests are very fire-resistant during the wet season due to high humidity. Models
377 trained over NHSA and EQAS show high relevance of relative humidity and temperature to

378 capture the climatic characteristics and their distinct seasonality (Figs S5d, m). The strong
379 influence of meteorological predictors are also noticeable over BONA and BOAS, especially
380 temperature contributes the most (12.3% and 16.4% respectively) (Figs S4a, j). These results are
381 associated with fire-climate interactions in boreal forests where fire frequency and extent are
382 affected depending on temperature variation (Hu et al., 2015; Kim et al., 2020) and their positive
383 feedbacks under climate change (Oris et al., 2014).

384

385 **4. Discussion & Conclusion**

386 In this study, we introduce a deep learning based fire model (DL-fire) and implement it
387 within the physics-based land surface model JSBACH4. The DL-fire predicts burnt fraction
388 based on weather conditions, land properties and anthropogenic effects, performing well in
389 predicting spatial and seasonal variation. When the DL-fire operates as a coupled module within
390 JSBACH4 (JSB4-DL-fire), the quality of fire damage simulation improves noticeably compared
391 to the simple fire scheme in JSBACH4. However, the predictability of JSB4-DL-fire is not as
392 accurate as the validation results of DL-fire forced by observation. Since the only differences
393 between the two are from land property predictors, either observed or simulated, its main reason
394 is presumed to be internal biases of JSBACH4.

395 To investigate the impact of JSBACH4 internal biases on fire prediction, we compare the
396 predictors from a validation dataset and the simulated by JSBACH4. In terms of global
397 perspective, the JSB4-DL-fire predictions overall underestimate fire damages from May to
398 September, and subsequently its rising and falling seasonal pattern is roughly a month lagged
399 from September to February (Fig S6). These similar discrepancies are found in LAI over Africa.
400 The simulated LAI in NHAF are overall underestimated with a month lagged peak in its
401 seasonality (Fig S7h). In SHAF, LAI shows opposite seasonal behavior from July to November
402 (Fig S7i), causing an underestimation of fire damage (Fig 4i).

403 Regionally, MIDE and SEAS show the most apparent discrepancies due to
404 overestimation in JSB4-DL-fire. JSBACH4 shows a tendency to underestimate water contents in
405 all the soil layers (Figs S8-11), except for the content of the first layer (SWL1) in MIDE (Fig
406 S8g). Considering that water availability in the topmost layer plays a vital role on vegetation

407 (Seneviratne et al., 2010) and agricultural productivity (Battista et al., 2016), the biases of SWL1
408 can mislead DL-fire to exaggerate combustible fuel amount or its conditions on the ground.
409 Similarly, overestimated durations of burnt fraction and LAI in SEAS coincide with each other
410 (Figs 4l and S7l). To effectively address internal biases of physics-based models, it was
411 suggested to merge deep learning as an external post-processing method (Reichstein et al., 2019;
412 Son et al., 2022). However, this approach is not directly applicable in this study due to dynamical
413 interactions between predictors and DGVMs. Instead, an online training approach, developing
414 the deep learning model concurrently with running DGVMs will be our next step to advance the
415 function of DL-fire in ESMs.

416 Representing interannual variability in global burnt area is yet a continuous effort for
417 improvement in fire-enable DGVMs. None of the DGVMs has yet proven to successfully
418 reproduce interannual variability (Hantson et al., 2020), and their limited skills cause
419 uncertainties for the global carbon budget estimation (Bastos et al., 2020). Previous DL model
420 showed ability to capture observed interannual patterns, but it is still early to assure its
421 preeminence due to its short evaluation period (Joshi & Sukumar, 2021). Although JSB4-DL-fire
422 either performs well at a global scale, significant regional improvements are observed with
423 higher than 0.7 of r_i over 6 out of 14 regions (Table 4). These results suggest that ML/DL based
424 hybrid approach can be a solution for the interannual variability problems in DGVMs.

425 Human influence fire regimes in various ways that either promote or limit fire. The
426 population growth and urban expansion generally increase fire incidents (Bowman et al., 2011),
427 whereas fire suppression and land-use changes decline fire activity (Andela et al., 2017). Our
428 model underrates roles of these factors showing conspicuously low global relevance (0.05%, Fig
429 5b). These consequences can be due to a coarse time resolution of anthropogenic dataset. Since
430 all the anthropogenic variables are interpolated from annual records or used as static values, they
431 cannot provide any information associated to seasonal variation or anomalous daily events.
432 Besides, some of the major man-made fire damages, particularly agricultural burnings, can be
433 explained by weather seasonality and vegetation states (Korontzi et al., 2006). However, it
434 should be pointed out that our model globally utilized C3 annual crops (c3ann) the most among
435 anthropogenic drivers (Fig S12a) to identify crop related activities, and regionally in NHAF,
436 BOAS, SEAS and EQAS (Fig S12i, k, m, n). Population follows as the second influential
437 anthropogenic factor and HDI also show relatively higher relevances in developed regions

438 (0.02% in TENA and 0.07% in EURO), echoing their socioeconomic impacts on fire (F. Li et al.,
439 2013; Teixeira et al., 2021). These results may suggest its potential of further improvement of
440 human impacts on fire activities with more sophisticated dataset and adapted model architecture.

441 Regarding a global or local training approach, it can be argued which one in particular is
442 a better option, either one single global model or multiple regional models. A global coverage
443 model can be efficient in terms of model development and coupling with DGVMs, but for it not
444 to lose regional characteristics, it may require more trainable parameters and higher complexity
445 in architecture. We tested to train a global model with the same architecture as our local models,
446 and its prediction accuracy significantly decreased ($r_m=0.1$). For the local approach, there are two
447 major points to be considered: 1) the number of regions that should be considered and, 2)
448 whether a unified or a specialized model design for each region should be developed.
449 Exploration of these options would enable us to further upgrade prediction performances,
450 however, this is not addressed in this study.

451 One of the main purposes of ESMs is to project climate changes based on future
452 scenarios. However, in this study, we decide not to project future fire regime changes with DL-
453 fire, although it is technically executable. This is because our model is currently composed of 14
454 regional models, and it cannot practically reflect global bioclimatic changes. Finally, we argue
455 that further approaches should focus on developing and training one global DL model coupled
456 with the host land surface model, and by that learning aspects of regional fire variability which
457 would support conducting fully hybrid projection simulations.

458

459 **Data Availability Statement**

460 GFED4 dataset is available at <https://www.globalfiredata.org/data.html>. Also, ERA5
461 dataset is available at <https://cds.climate.copernicus.eu/cdsapp#!/home>, lightning climatology
462 dataset (LIS-OTD) is available at <https://ghrc.nsstc.nasa.gov/pub/lis/climatology/>, LAI dataset
463 from MODIS is available at
464 <https://ladsweb.modaps.eosdis.nasa.gov/archive/allData/6/MCD15A3H/>, Topography dataset is
465 available at <https://doi.pangaea.de/10.1594/PANGAEA.867114>, HYDE3.2 dataset is available at
466 <https://www.pbl.nl/en/image/links/hyde>, GDP and HDI dataset is available at

467 <https://datadryad.org/stash/dataset/doi:10.5061/dryad.dk1j0>, GRIP4 dataset is available at
 468 <https://www.globio.info/download-grip-dataset>, LUH2 dataset is available at
 469 <https://luh.umd.edu/>. Also, the model simulation results are openly available in Zenodo at
 470 <https://doi.org/10.5281/zenodo.7728155>.

471 Acknowledgments

472 This work was supported by the European Union’s H2020 research and innovation programme
 473 under grant agreement nos. 101003536 (ESM2025). We should secondly acknowledge SeasFire
 474 (Lazaro), DeepCube (Christian) and USMILE (Alex).

475

476 References

- 477 Amatulli, G., Domisch, S., Tuanmu, M.-N., Parmentier, B., Ranipeta, A., Malczyk, J., & Jetz, W. (2018). A suite of
 478 global, cross-scale topographic variables for environmental and biodiversity modeling. *Scientific Data*, *5*(1),
 479 1–15.
- 480 Andela, N., Morton, D. C., Giglio, L., Chen, Y., van der Werf, G. R., Kasibhatla, P. S., DeFries, R. S., Collatz, G. J.,
 481 Hantson, S., & Kloster, S. (2017). A human-driven decline in global burned area. *Science*, *356*(6345), 1356–
 482 1362.
- 483 Bach, S., Binder, A., Montavon, G., Klauschen, F., Müller, K.-R., & Samek, W. (2015). On pixel-wise explanations
 484 for non-linear classifier decisions by layer-wise relevance propagation. *PLoS One*, *10*(7), e0130140.
- 485 Bastos, A., O’Sullivan, M., Ciais, P., Makowski, D., Sitch, S., Friedlingstein, P., Chevallier, F., Rödenbeck, C.,
 486 Pongratz, J., & Luijkx, I. T. (2020). Sources of uncertainty in regional and global terrestrial CO₂ exchange
 487 estimates. *Global Biogeochemical Cycles*, *34*(2), e2019GB006393.
- 488 Battista, P., Chiesi, M., Rapi, B., Romani, M., Cantini, C., Giovannelli, A., Coccozza, C., Tognetti, R., & Maselli, F.
 489 (2016). Integration of ground and multi-resolution satellite data for predicting the water balance of a
 490 Mediterranean two-layer agro-ecosystem. *Remote Sensing*, *8*(9), 731.
- 491 Bowman, D. M. J. S., Balch, J., Artaxo, P., Bond, W. J., Cochrane, M. A., D’Antonio, C. M., DeFries, R., Johnston,
 492 F. H., Keeley, J. E., & Krawchuk, M. A. (2011). The human dimension of fire regimes on Earth. *Journal of*
 493 *Biogeography*, *38*(12), 2223–2236.
- 494 Carcaillet, C., Almquist, H., Asnong, H., Bradshaw, R. H. W., Carrion, J. S., Gaillard, M.-J., Gajewski, K., Haas, J.
 495 N., Haberle, S. G., & Hadorn, P. (2002). Holocene biomass burning and global dynamics of the carbon cycle.
 496 *Chemosphere*, *49*(8), 845–863.
- 497 Cecil, D. J., Buechler, D. E., & Blakeslee, R. J. (2014). Gridded lightning climatology from TRMM-LIS and OTD:
 498 Dataset description. *Atmospheric Research*, *135*, 404–414.
- 499 Coughlan, R., di Giuseppe, F., Vitolo, C., Barnard, C., Lopez, P., & Drusch, M. (2021). Using machine learning to
 500 predict fire-ignition occurrences from lightning forecasts. *Meteorological Applications*, *28*(1), e1973.
- 501 Crutzen, P. J., & Andreae, M. O. (1990). Biomass burning in the tropics: Impact on atmospheric chemistry and
 502 biogeochemical cycles. *Science*, *250*(4988), 1669–1678.
- 503 D’Este, M., Elia, M., Giannico, V., Spano, G., Laforteza, R., & Sanesi, G. (2021). Machine learning techniques for
 504 fine dead fuel load estimation using multi-source remote sensing data. *Remote Sensing*, *13*(9), 1658.
- 505 Drüke, M., Forkel, M., von Bloh, W., Sakschewski, B., Cardoso, M., Bustamante, M., Kurths, J., & Thonicke, K.
 506 (2019). Improving the LPJmL4-SPITFIRE vegetation–fire model for South America using satellite data.
 507 *Geoscientific Model Development*, *12*(12), 5029–5054.
- 508 Dugas, C., Bengio, Y., Bélisle, F., Nadeau, C., & Garcia, R. (2000). Incorporating second-order functional
 509 knowledge for better option pricing. *Advances in Neural Information Processing Systems*, *13*.
- 510 Forkel, M., Andela, N., Harrison, S. P., Lasslop, G., van Marle, M., Chuvieco, E., Dorigo, W., Forrest, M., Hantson,
 511 S., & Heil, A. (2019). Emergent relationships with respect to burned area in global satellite observations and
 512 fire-enabled vegetation models. *Biogeosciences*, *16*(1), 57–76.

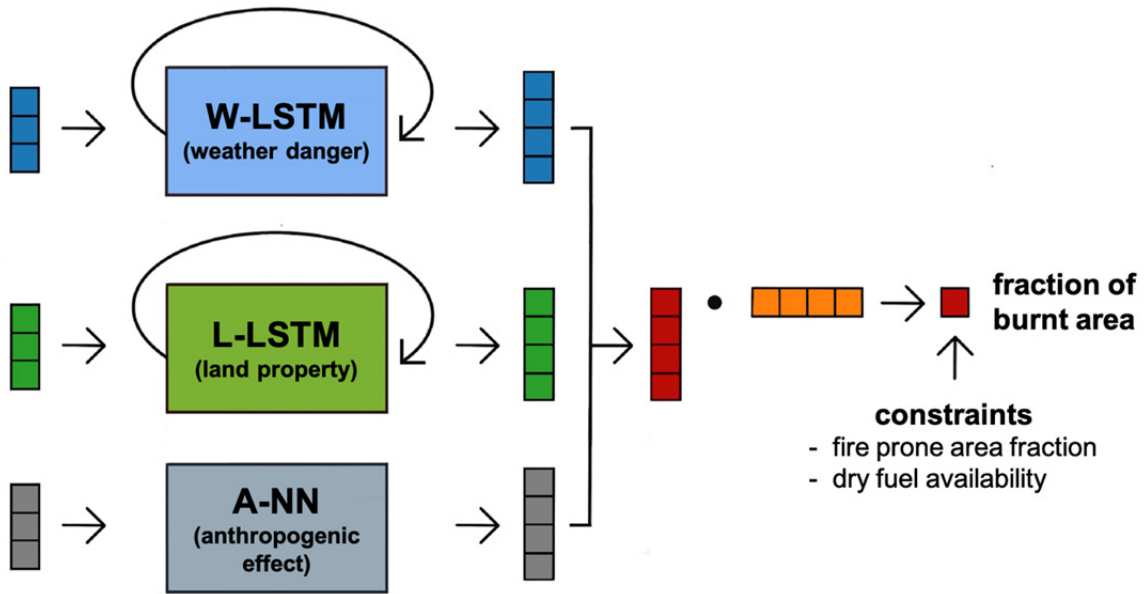
- 513 Hantson, S., Arneth, A., Harrison, S. P., Kelley, D. I., Prentice, I. C., Rabin, S. S., Archibald, S., Mouillot, F.,
 514 Arnold, S. R., Artaxo, P., Bachelet, D., Ciais, P., Forrest, M., Friedlingstein, P., Hickler, T., Kaplan, J. O.,
 515 Kloster, S., Knorr, W., Lasslop, G., ... Yue, C. (2016). The status and challenge of global fire modelling.
 516 *Biogeosciences*, *13*(11), 3359–3375. <https://doi.org/10.5194/bg-13-3359-2016>
- 517 Hantson, S., Kelley, D. I., Arneth, A., Harrison, S. P., Archibald, S., Bachelet, D., Forrest, M., Hickler, T., Lasslop,
 518 G., & Li, F. (2020). Quantitative assessment of fire and vegetation properties in simulations with fire-enabled
 519 vegetation models from the Fire Model Intercomparison Project. *Geoscientific Model Development*, *13*(7),
 520 3299–3318.
- 521 Hardouin, L., Delire, C., Decharme, B., Lawrence, D. M., Nabel, J. E. M. S., Brovkin, V., Collier, N., Fisher, R.,
 522 Hoffman, F. M., & Koven, C. D. (2022). Uncertainty in land carbon budget simulated by terrestrial biosphere
 523 models: the role of atmospheric forcing. *Environmental Research Letters*, *17*(9), 094033.
- 524 Harrison, S. P., Bartlein, P. J., Brovkin, V., Houweling, S., Kloster, S., & Prentice, I. C. (2018). The biomass
 525 burning contribution to climate–carbon-cycle feedback. *Earth System Dynamics*, *9*(2), 663–677.
- 526 Hersbach, H., Bell, B., Berrisford, P., Hirahara, S., Horányi, A., Muñoz-Sabater, J., Nicolas, J., Peubey, C., Radu,
 527 R., & Schepers, D. (2020). The ERA5 global reanalysis. *Quarterly Journal of the Royal Meteorological
 528 Society*, *146*(730), 1999–2049.
- 529 Hochreiter, S., & Schmidhuber, J. (1997). Long short-term memory. *Neural Computation*, *9*(8), 1735–1780.
- 530 Hodges, J. L., & Lattimer, B. Y. (2019). Wildland fire spread modeling using convolutional neural networks. *Fire
 531 Technology*, *55*(6), 2115–2142.
- 532 Hu, F. S., Higuera, P. E., Duffy, P., Chipman, M. L., Rocha, A. v., Young, A. M., Kelly, R., & Dietze, M. C. (2015).
 533 Arctic tundra fires: natural variability and responses to climate change. *Frontiers in Ecology and the
 534 Environment*, *13*(7), 369–377.
- 535 Hurtt, G. C., Chini, L., Sahajpal, R., Frothingham, S., Bodirsky, B. L., Calvin, K., Doelman, J. C., Fisk, J., Fujimori, S.,
 536 & Klein Goldewijk, K. (2020). Harmonization of global land use change and management for the period 850–
 537 2100 (LUH2) for CMIP6. *Geoscientific Model Development*, *13*(11), 5425–5464.
- 538 Joshi, J., & Sukumar, R. (2021). Improving prediction and assessment of global fires using multilayer neural
 539 networks. *Scientific Reports*, *11*(1), 1–14.
- 540 Jungclaus, J. H., Lorenz, S. J., Schmidt, H., Brovkin, V., Brüggemann, N., Chegini, F., Crüger, T., De-Vrese, P.,
 541 Gayler, V., & Giorgetta, M. A. (2022). The ICON earth system model version 1.0. *Journal of Advances in
 542 Modeling Earth Systems*, *14*(4), e2021MS002813.
- 543 Kelley, D. I., Prentice, I. C., Harrison, S. P., Wang, H., Simard, M., Fisher, J. B., & Willis, K. O. (2013). A
 544 comprehensive benchmarking system for evaluating global vegetation models. *Biogeosciences*, *10*(5), 3313–
 545 3340.
- 546 Kim, J.-S., Kug, J.-S., Jeong, S.-J., Park, H., & Schaepman-Strub, G. (2020). Extensive fires in southeastern
 547 Siberian permafrost linked to preceding Arctic Oscillation. *Science Advances*, *6*(2), eaax3308.
- 548 Kingma, D. P., & Ba, J. (2014). Adam: A method for stochastic optimization. *ArXiv Preprint ArXiv:1412.6980*.
- 549 Klein Goldewijk, K., Beusen, A., Doelman, J., & Stehfest, E. (2017). Anthropogenic land use estimates for the
 550 Holocene–HYDE 3.2. *Earth System Science Data*, *9*(2), 927–953.
- 551 Kloster, S., Mahowald, N. M., Randerson, J. T., Thornton, P. E., Hoffman, F. M., Levis, S., Lawrence, P. J.,
 552 Feddema, J. J., Oleson, K. W., & Lawrence, D. M. (2010). Fire dynamics during the 20th century simulated by
 553 the Community Land Model. *Biogeosciences*, *7*(6), 1877–1902.
- 554 Koppmann, R., von Czapiewski, K., & Reid, J. S. (2005). A review of biomass burning emissions, part I: gaseous
 555 emissions of carbon monoxide, methane, volatile organic compounds, and nitrogen containing compounds.
 556 *Atmospheric Chemistry and Physics Discussions*, *5*(5), 10455–10516.
- 557 Korontzi, S., McCarty, J., Loboda, T., Kumar, S., & Justice, C. (2006). Global distribution of agricultural fires in
 558 croplands from 3 years of Moderate Resolution Imaging Spectroradiometer (MODIS) data. *Global
 559 Biogeochemical Cycles*, *20*(2).
- 560 Kummu, M., Taka, M., & Guillaume, J. H. A. (2018). Gridded global datasets for gross domestic product and
 561 Human Development Index over 1990–2015. *Scientific Data*, *5*(1), 1–15.
- 562 Kurz, W. A., Apps, M. J., Stocks, B. J., & Volney, W. J. A. (1995). Global climate change: disturbance regimes and
 563 biospheric feedbacks of temperate and boreal forests. *Biotic Feedbacks in the Global Climatic System: Will
 564 the Warming Feed the Warming*, 119–133.
- 565 Lasslop, G., Thonicke, K., & Kloster, S. (2014). SPITFIRE within the MPI Earth system model: Model
 566 development and evaluation. *Journal of Advances in Modeling Earth Systems*, *6*(3), 740–755.
- 567 le Page, Y., Morton, D., Bond-Lamberty, B., Pereira, J. M. C., & Hurtt, G. (2015). HESFIRE: a global fire model to
 568 explore the role of anthropogenic and weather drivers. *Biogeosciences*, *12*(3), 887–903.

- 569 Lenihan, J. M. (1998). Simulating broad-scale fire severity in a dynamic global vegetation model. *Northwest Sci.*,
570 72(2), 91–103.
- 571 Li, F., Lawrence, D. M., & Bond-Lamberty, B. (2017). Impact of fire on global land surface air temperature and
572 energy budget for the 20th century due to changes within ecosystems. *Environmental Research Letters*, 12(4),
573 44014.
- 574 Li, F., Levis, S., & Ward, D. S. (2013). Quantifying the role of fire in the Earth system—Part 1: Improved global fire
575 modeling in the Community Earth System Model (CESM1). *Biogeosciences*, 10(4), 2293–2314.
- 576 Li, Z., Huang, Y., Li, X., & Xu, L. (2021). Wildland fire burned areas prediction using long short-term memory
577 neural network with attention mechanism. *Fire Technology*, 57(6), 1–23.
- 578 Liang, H., Zhang, M., & Wang, H. (2019). A neural network model for wildfire scale prediction using
579 meteorological factors. *IEEE Access*, 7, 176746–176755.
- 580 Liu, Z., Ballantyne, A. P., & Cooper, L. A. (2019). Biophysical feedback of global forest fires on surface
581 temperature. *Nature Communications*, 10(1), 1–9.
- 582 López-Saldaña, G., Bistinas, I., & Pereira, J. M. C. (2015). Global analysis of radiative forcing from fire-induced
583 shortwave albedo change. *Biogeosciences*, 12(2), 557–565.
- 584 Mahowald, N. (2011). Aerosol indirect effect on biogeochemical cycles and climate. *Science*, 334(6057), 794–796.
- 585 McLauchlan, K. K., Higuera, P. E., Miesel, J., Rogers, B. M., Schweitzer, J., Shuman, J. K., Tepley, A. J., Varner, J.
586 M., Veblen, T. T., & Adalsteinsson, S. A. (2020). Fire as a fundamental ecological process: Research
587 advances and frontiers. *Journal of Ecology*, 108(5), 2047–2069.
- 588 Meijer, J. R., Huijbregts, M. A. J., Schotten, K. C. G. J., & Schipper, A. M. (2018). Global patterns of current and
589 future road infrastructure. *Environmental Research Letters*, 13(6), 064006.
- 590 Muñoz-Sabater, J., Dutra, E., Agustí-Panareda, A., Albergel, C., Arduini, G., Balsamo, G., Boussetta, S., Choulga,
591 M., Harrigan, S., & Hersbach, H. (2021). ERA5-Land: A state-of-the-art global reanalysis dataset for land
592 applications. *Earth System Science Data*, 13(9), 4349–4383.
- 593 Myneni, R., Knyazikhin, Y., Park, T., & SIPS-NASA, B. U. and M. (2015). MOD15A3H MODIS/Combined Terra+
594 Aqua Leaf Area Index/FPAR Daily L4 Global 500m SIN Grid. In *NASA LP DAAC*.
- 595 Oris, F., Asselin, H., Ali, A. A., Finsinger, W., & Bergeron, Y. (2014). Effect of increased fire activity on global
596 warming in the boreal forest. *Environmental Reviews*, 22(3), 206–219.
- 597 Pfeiffer, M., Spessa, A., & Kaplan, J. O. (2013). A model for global biomass burning in preindustrial time: LPJ-
598 LMfire (v1. 0). *Geoscientific Model Development*, 6(3), 643–685.
- 599 Pongratz, J., Reick, C., Raddatz, T., & Claussen, M. (2008). A reconstruction of global agricultural areas and land
600 cover for the last millennium. *Global Biogeochemical Cycles*, 22(3).
- 601 Radke, D., Hessler, A., & Ellsworth, D. (2019). FireCast: Leveraging Deep Learning to Predict Wildfire Spread.
602 *IJCAI*, 4575–4581.
- 603 Randerson, J. T., van der Werf, G. R., Giglio, L., Collatz, G. J., & Kasibhatla, P. S. (2015). Global fire emissions
604 database, version 4.1 (GFEDv4). *ORNL DAAC*.
- 605 Reichstein, M., Camps-Valls, G., Stevens, B., Jung, M., Denzler, J., & Carvalhais, N. (2019). Deep learning and
606 process understanding for data-driven Earth system science. *Nature*, 566(7743), 195–204.
- 607 Reick, C. H., Gayler, V., Goll, D., Hagemann, S., Heidkamp, M., Nabel, J. E. M. S., Raddatz, T., Roeckner, E.,
608 Schnur, R., & Wilkenskield, S. (2021). *JSBACH 3-The land component of the MPI Earth System Model:
609 documentation of version 3.2*.
- 610 Rothermel, R. C. (1972). *A mathematical model for predicting fire spread in wildland fuels* (Vol. 115).
611 Intermountain Forest & Range Experiment Station, Forest Service, US
- 612 Seidl, R., Thom, D., Kautz, M., Martin-Benito, D., Peltoniemi, M., Vacchiano, G., Wild, J., Ascoli, D., Petr, M., &
613 Honkaniemi, J. (2017). Forest disturbances under climate change. *Nature Climate Change*, 7(6), 395–402.
- 614 Seneviratne, S. I., Corti, T., Davin, E. L., Hirschi, M., Jaeger, E. B., Lehner, I., Orlowsky, B., & Teuling, A. J.
615 (2010). Investigating soil moisture–climate interactions in a changing climate: A review. *Earth-Science
616 Reviews*, 99(3–4), 125–161.
- 617 Shi, X., Chen, Z., Wang, H., Yeung, D.-Y., Wong, W.-K., & Woo, W. (2015). Convolutional LSTM network: A
618 machine learning approach for precipitation nowcasting. *Advances in Neural Information Processing Systems*,
619 28.
- 620 Son, R., Kim, H., Wang, S.-Y. S., Jeong, J.-H., Woo, S.-H., Jeong, J.-Y., Lee, B.-D., Kim, S. H., LaPlante, M., &
621 Kwon, C.-G. (2021). Changes in fire weather climatology under 1.5° C and 2.0° C warming. *Environmental
622 Research Letters*, 16(3), 34058.

- 623 Son, R., Ma, P., Wang, H., Rasch, P. J., Wang, S., Kim, H., Jeong, J., Lim, K. S., & Yoon, J. (2022). Deep Learning
624 provides substantial improvements to county-level fire weather forecasting over the western United States.
625 *Journal of Advances in Modeling Earth Systems*, e2022MS002995.
- 626 Teixeira, J. C., Folberth, G. A., O'Connor, F. M., Unger, N., & Voulgarakis, A. (2021). Coupling interactive fire
627 with atmospheric composition and climate in the UK Earth System Model. *Geoscientific Model Development*,
628 14(10), 6515–6539.
- 629 Thonicke, K., Spessa, A., Prentice, I. C., Harrison, S. P., Dong, L., & Carmona-Moreno, C. (2010). The influence of
630 vegetation, fire spread and fire behaviour on biomass burning and trace gas emissions: results from a process-
631 based model. *Biogeosciences*, 7(6), 1991–2011.
- 632 Thonicke, K., Venevsky, S., Sitch, S., & Cramer, W. (2001). The role of fire disturbance for global vegetation
633 dynamics: coupling fire into a Dynamic Global Vegetation Model. *Global Ecology and Biogeography*, 10(6),
634 661–677.
- 635 van der Werf, G. R., Randerson, J. T., Giglio, L., van Leeuwen, T. T., Chen, Y., Rogers, B. M., Mu, M., van Marle,
636 M. J. E., Morton, D. C., & Collatz, G. J. (2017). Global fire emissions estimates during 1997–2016. *Earth
637 System Science Data*, 9(2), 697–720.
- 638 Venevsky, S., Thonicke, K., Sitch, S., & Cramer, W. (2002). Simulating fire regimes in human-dominated
639 ecosystems: Iberian Peninsula case study. *Global Change Biology*, 8(10), 984–998.
- 640 Voulgarakis, A., & Field, R. D. (2015). Fire influences on atmospheric composition, air quality and climate. *Current
641 Pollution Reports*, 1(2), 70–81.
- 642 Ward, D. S., Kloster, S., Mahowald, N. M., Rogers, B. M., Randerson, J. T., & Hess, P. G. (2012). The changing
643 radiative forcing of fires: global model estimates for past, present and future. *Atmospheric Chemistry and
644 Physics*, 12(22), 10857–10886.
- 645 Yue, C., Ciais, P., Zhu, D., Wang, T., Peng, S. S., & Piao, S. L. (2016). How have past fire disturbances contributed
646 to the current carbon balance of boreal ecosystems? *Biogeosciences*, 13(3), 675–690.
- 647 Zhang, G., Wang, M., & Liu, K. (2021). Deep neural networks for global wildfire susceptibility modelling.
648 *Ecological Indicators*, 127, 107735.
- 649 Zhu, Q., Li, F., Riley, W. J., Xu, L., Zhao, L., Yuan, K., Wu, H., Gong, J., & Randerson, J. (2022). Building a
650 machine learning surrogate model for wildfire activities within a global Earth system model. *Geoscientific
651 Model Development*, 15(5), 1899–1911.
- 652
653
654
655
656
657
658
659
660
661
662
663
664
665
666
667
668
669
670
671
672
673

674
675
676
677
678

Figures and Tables

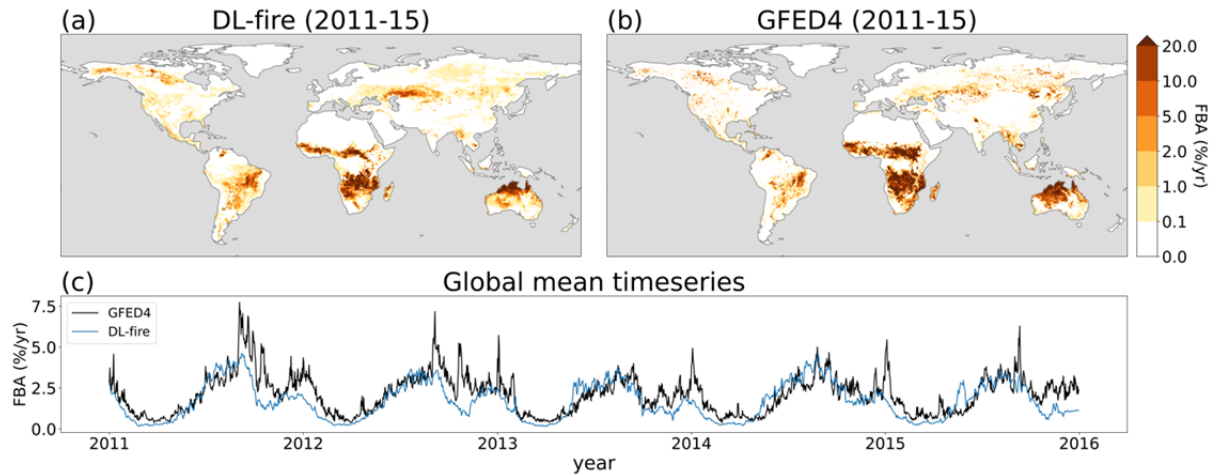


679
680

Figure 1. Flowchart of DL-fire model.

681
682
683
684
685
686
687
688
689
690
691
692
693
694
695
696
697
698
699
700
701
702

703
704
705

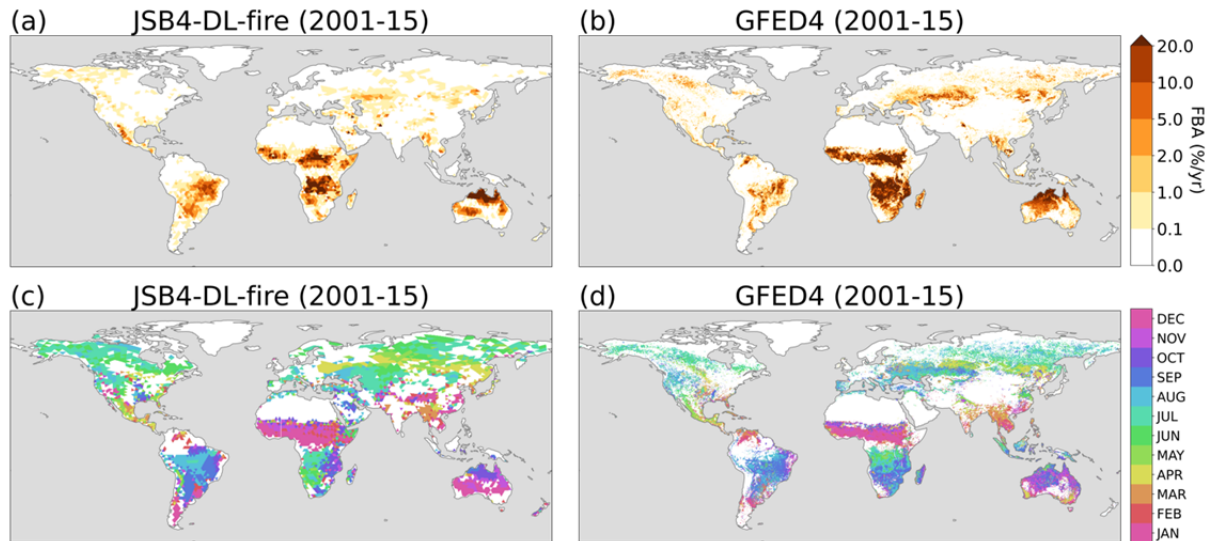


706
707
708
709
710

Figure 2. Spatial and temporal comparison between and GFED4 and DL-fire predictions. The maps of **a.** DL-fire and **b.** GFED4 visualize annual burnt fraction averaged over evaluation period (2011-15). **c.** compares global mean of burnt fraction from GFED4 (black) and DL-fire (blue).

711
712
713
714
715
716
717
718
719
720
721
722
723
724
725
726
727
728
729
730
731
732
733
734
735
736

737
738
739

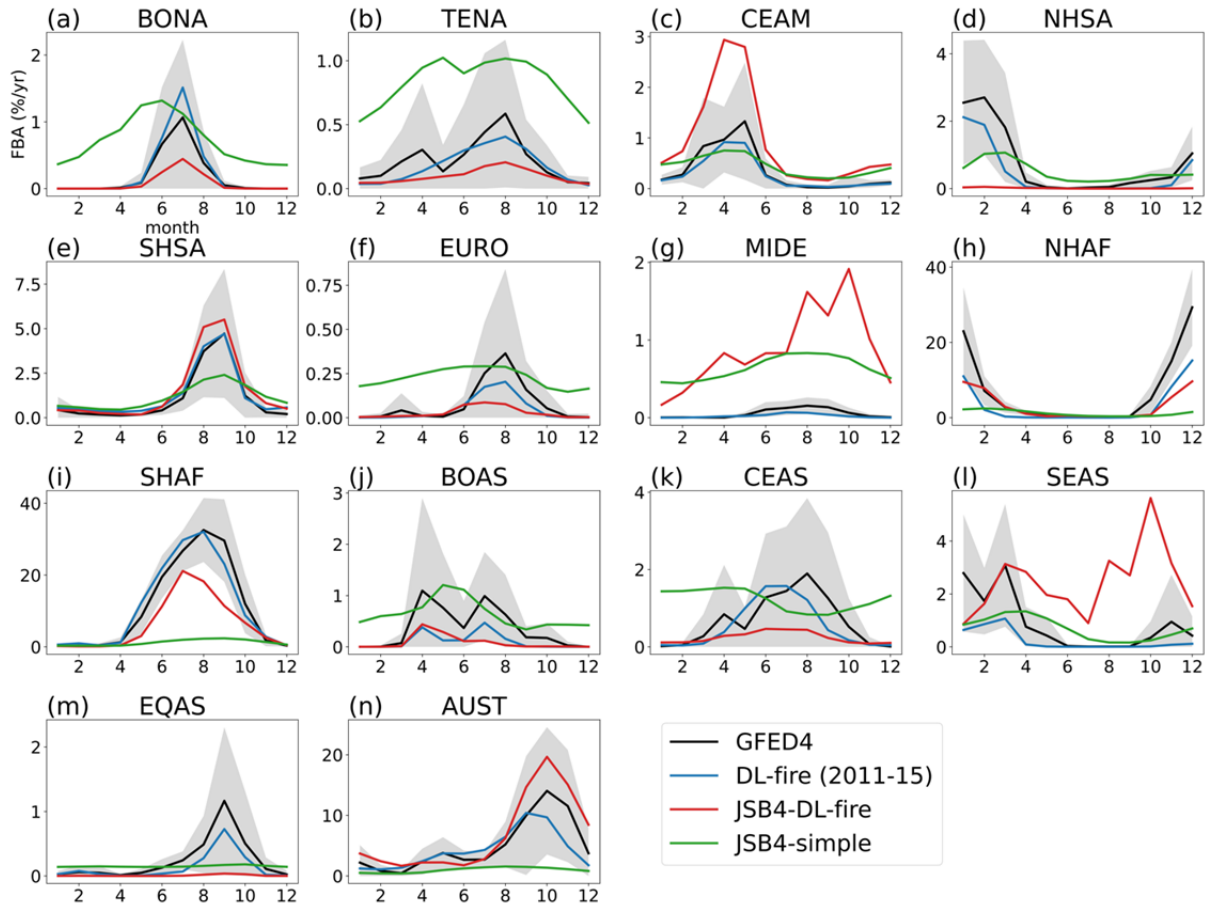


740
741
742
743
744

Figure 3. Spatial maps of burnt fraction and its seasonality. The maps on the top (**a.** JSB4-DL-fire and **b.** GFED4) show annual burnt fraction averaged over the years 2001-15, and the bottoms (**c.** JSB4-DL-fire and **d.** GFED4) visualize the peak month of burnt fraction. All areas with annual burnt fraction less than 0.1%/yr are masked out (white).

745
746
747
748
749
750
751
752
753
754
755
756
757
758
759
760
761
762
763
764
765
766
767
768

769
770
771

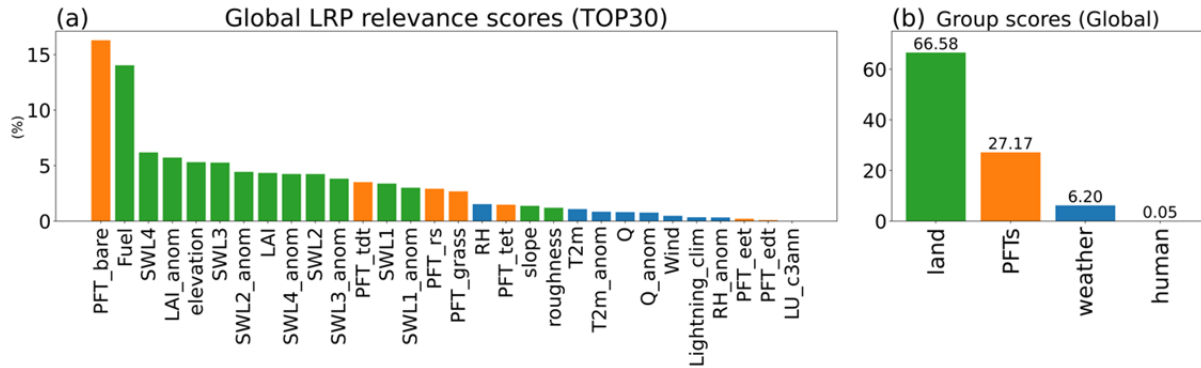


772
773
774
775
776

Figure 4. Comparison of monthly mean burnt fraction. Burnt fractions for GFED4 (black), JSB4-DL-fire (red), JSB4-simple (green) during 2001-15 and DL-fire (blue) during 2011-15 are averaged for each month and compared on each GFED regions (Figure S1). Gray shadings indicate 1-sigma intervals of the GFED4.

777
778
779
780
781
782
783
784
785
786
787
788
789
790

791
792
793



794
795
796
797
798
799

Figure 5. Global predictor importance assessment. **a.** shows predictors with the highest 30 LRP relevance scores and they are color-coded in four groups: weather conditions (blue), land properties (green), anthropogenic effects (gray) and PFTs (orange). Full names of PFTs and land use states (LU) are in Table 2 and Table S1. **b.** compares the relevance between the groups and their scores are displayed on top of bars.

800
801
802
803
804
805
806
807
808
809
810
811
812
813
814
815
816
817
818
819
820
821
822
823
824
825
826
827

828
829
830
831
832

Table 1. Ratio between grid-cell level fire/no-fire incidents per region. The last column is for downsampling ratios used for step2.

	fire:no-fire	step1	step2	ratio (step2)
BONA	1:1313	1:301	1:1.0	300
TENA	1:412	1:61	1:1.23	50
CEAM	1:122	1:23	1:1.16	20
NHSA	1:85	1:20	1:1.02	20
SHSA	1:72	1:15	1:1.53	10
EURO	1:988	1:149	1:1.49	100
MIDE	1:1023	1:188	1:1.88	100
NHAF	1:27	1:8.4	1:1.69	5
SHAF	1:12	1:4.0	1:0.99	5
BOAS	1:721	1:128	1:1.27	100
CEAS	1:188	1:32	1:1.06	30
SEAS	1:104	1:24	1:1.19	20
EQAS	1:180	1:29	1:1.43	20
AUST	1:75	1:18	1:1.78	10

833
834
835
836
837
838
839
840
841
842
843
844
845
846
847
848
849
850
851
852

853
854
855
856
857

Table 2. Model input predictors.

Weather danger (W-LSTM)	temperature	ERA5 (Hersbach et al., 2020)
	temperature anomaly	
	specific/relative humidity	
	specific/relative humidity anomaly	
	wind speed	
	precipitation	
	lightning climatology	
	volume of water in soil layers (4 levels) lv1: 0-7cm, lv2: 7-28cm, lv3: 28-100cm, lv4: 100-289cm	ERA5
	volume of water anomaly (4 levels)	
	LAI	MODIS
	LAI anomaly	(Myneni et al., 2015)
	elevation	
	slope	(Amatulli et al., 2018)
	roughness	
Land property (L-LSTM)	fuel (above ground plant litter)	JSBACH4
	fraction of 9 plant functional types (PFTs) - snow (PFT_snow) - tropical evergreen trees (PFT_tet) - tropical deciduous trees (PFT_tdt) - extra-tropical evergreen trees (PFT_eet) - extra-tropical deciduous trees (PFT_edt) - raingreen shrubs (PFT_rs) - deciduous shrubs (PFT_ds) - grass (PFT_grass) - bare land (PFT_bare)	(Pongratz et al., 2008)
		HYDE3.2
Anthropogenic effect (A-NN)	population density	(Klein Goldewijk et al., 2017)
	gross domestic product (GDP)	(Kummu et al., 2018)
	human development index (HDI)	

total road density	GRIP4 (Meijer et al., 2018)
land use (14) states (Table S1)	LUH2 (Hurtt et al., 2020)

858 **Table 3.** Evaluation metric scores for DL-fire.

	NME	MPD	r_d	r_m	r_i
Global	0.64	0.30	0.73	0.80	0.35
BONA	0.90	0.36	0.81	0.95	0.92
TENA	0.77	0.35	0.47	0.64	0.92
CEAM	0.72	0.19	0.82	0.90	0.86
NHSA	0.48	0.31	0.74	0.85	0.85
SHSA	0.83	0.23	0.85	0.89	0.52
EURO	0.76	0.33	0.60	0.76	0.92
MIDE	0.49	0.31	0.62	0.72	0.30
NHAF	0.58	0.31	0.88	0.93	0.38
SHAF	0.96	0.33	0.90	0.94	0.08
BOAS	0.69	0.31	0.63	0.77	0.82
CEAS	0.86	0.39	0.41	0.55	0.97
SEAS	0.56	0.22	0.60	0.82	-0.14
EQAS	0.55	0.28	0.90	0.97	0.99
AUST	0.50	0.29	0.66	0.76	0.50

859
860
861
862
863
864
865
866
867
868
869
870
871
872
873
874
875

876
 877
 878
 879
 880
 881
 882

Table 4. Evaluation metric scores for JSB4-DL-fire (JSB4-simple).

	NME	MPD	r_d	r_m	r_i
Global	0.67 (0.75)	0.31 (0.30)	0.61 (-0.07)	0.79 (-0.07)	0.37 (0.17)
BONA	0.72 (2.34)	0.36 (0.34)	0.62 (0.45)	0.85 (0.56)	0.71 (0.44)
TENA	0.71 (2.49)	0.35 (0.28)	0.37 (0.32)	0.64 (0.48)	0.82 (0.82)
CEAM	1.53 (1.08)	0.19 (0.24)	0.70 (0.61)	0.82 (0.72)	0.62 (0.37)
NHSA	0.61 (0.68)	0.21 (0.21)	0.55 (0.61)	0.72 (0.71)	0.51 (0.53)
SHSA	0.83 (0.85)	0.21 (0.20)	0.81 (0.71)	0.89 (0.77)	0.78 (0.62)
EURO	0.70 (2.06)	0.38 (0.36)	0.29 (0.32)	0.55 (0.50)	0.34 (0.32)
MIDE	7.96 (6.10)	0.32 (0.31)	0.12 (0.61)	0.34 (0.75)	-0.12 (-0.18)
NHAF	0.58 (0.67)	0.37 (0.44)	0.75 (0.35)	0.87 (0.39)	0.80 (0.65)
SHAF	0.76 (0.82)	0.33 (0.28)	0.84 (0.80)	0.91 (0.86)	0.35 (0.14)
BOAS	0.68 (1.40)	0.35 (0.36)	0.60 (0.27)	0.78 (0.35)	0.76 (0.10)
CEAS	0.61 (1.39)	0.39 (0.32)	0.57 (-0.24)	0.67 (-0.32)	0.29 (-0.22)
SEAS	2.05 (0.88)	0.25 (0.19)	-0.02 (0.40)	-0.03 (0.54)	-0.04 (0.32)
EQAS	0.50 (0.81)	0.25 (0.26)	0.41 (0.63)	0.77 (0.74)	0.80 (0.90)
AUST	0.81 (0.72)	0.26 (0.33)	0.70 (0.48)	0.78 (0.55)	0.42 (0.62)

883